

Quantum-classical correspondence for spins at finite temperatures with application to Monte Carlo simulations

A. El Mendili¹ and M. E. Zhitomirsky^{1, 2}

¹Université Grenoble Alpes, CEA, IRIG, PHELIQS, 38000 Grenoble, France

²Institut Laue Langevin, 38042 Grenoble Cedex 9, France

(Dated: February 19, 2026)

We consider quantum-to-classical mapping for an arbitrary system of interacting spins at finite temperatures. We prove that, in the large- S limit, the asymptotic form of the partition function coincides with that of a classical model for spins of length $S_C = \sqrt{S(S+1)}$. Quantum corrections to the leading term form a series in powers of $1/[S(S+1)]$. This representation provides a rigorous basis for classical modeling of realistic magnetic Hamiltonians. As an application, the classical Monte Carlo simulations are performed to compute transition temperatures for several topical materials with known interaction parameters, including MnF_2 , MnTe , Rb_2MnF_4 , MnPSe_3 , FePS_3 , FePSe_3 , CoPS_3 , CrSBr , and CrI_3 . The resulting transition temperatures show good agreement with experimental data.

I. INTRODUCTION

The ever-growing demand for magnetic applications fuels interest in the theoretical modeling of relevant materials across a wide range of temperatures. Significant progress has been made in recent years in the experimental determination [1–14] and the theoretical computation [15, 16] of microscopic interactions in magnetic solids, providing realistic spin models for their description. The thermodynamics of quantum magnets including their phase transitions can be studied using powerful quantum Monte Carlo (MC) methods [17, 18]. Nevertheless, many realistic spin models exhibit some form of magnetic frustration, which stems from either lattice geometry or weak competing interactions. The presence of magnetic frustration leads to the negative sign problem that precludes efficient quantum simulations [18]. In contrast, the classical MC simulations [19] can conveniently incorporate the full complexity of microscopic interactions in magnetic solids. This naturally raises the question of the validity of classical numerical methods applied to the study of quantum spin models.

From a general standpoint [20, 21], quantum spins should behave more classically with increasing spin quantum number. In magnetism, one typically deals with interacting spin models described in the simplest case by the Heisenberg exchange Hamiltonian:

$$\hat{\mathcal{H}} = \sum_{\langle ij \rangle} J_{ij} \mathbf{S}_i \cdot \mathbf{S}_j - H \sum_i S_i^z. \quad (1)$$

Here \mathbf{S}_j are spin- S operators, J_{ij} are exchange coupling constants, and H is a dimensionless magnetic field. A usual way to obtain the semiclassical form of (1) consists in transforming to the rescaled operators $\mathbf{s}_j = \mathbf{S}_j/S$, which obey the commutation relations

$$[s_j^\alpha, s_k^\beta] = \frac{i}{S} e^{\alpha\beta\gamma} s_j^\gamma \delta_{jk}. \quad (2)$$

In the limit $S \rightarrow \infty$, the commutators vanish and \mathbf{s}_j become the classical unit vectors [22–24]. Accordingly,

the exchange parameter(s) J_C and an applied magnetic field H_C for the classical model are obtained from the original model (1) by a substitution

$$J_C = JS^2, \quad H_C = HS. \quad (3)$$

The spin-wave theory, regardless of whether the bosonic [25] or path-integral formulation [26] is used, comes up with essentially the same quantum-to-classical mapping. In particular, the spin dependence defined by (3) holds for the exact ground-state energy of an exchange ferromagnet. Additionally, the relation $H \simeq JS$ applies to the transition fields in antiferromagnets at $T = 0$, including an exact expression for the saturation field.

The question about the quantum-classical correspondence for the *statistical* properties of quantum spin systems was originally raised by Elliott Lieb in 1973 [27]. He proved a remarkable theorem stating that for the exchange Hamiltonian (1) the quantum partition function $Z_Q(S)$ and the partition function $Z_C(x)$ for classical spins of length x obey the following inequalities:

$$Z_C(S) \leq Z_Q(S) \leq Z_C(S+1), \quad (4)$$

which, in turn, provide the free-energy bounds

$$F_C(S+1) \leq F_Q(S) \leq F_C(S). \quad (5)$$

Accordingly, the length S_C of classical vectors chosen to represent quantum spins in the large- S limit have to obey

$$S \leq S_C \leq (S+1). \quad (6)$$

At $T = 0$, the spin-wave theory yields $S_C = S$, but such a choice may not necessarily be correct for all temperatures. Indeed, in order to match the Curie constant, classical spins must have $S_C = \sqrt{S(S+1)}$, which is also consistent with (6). Another justification for such substitution comes from the sum rule for the dynamical structure factor [28, 29].

Numerical consistency of the quantum-classical correspondence with $S_C = \sqrt{S(S+1)}$ has been addressed in

several studies. Oitmaa and Zheng [30] used the high-temperature series expansion for computing transition temperatures T_c for the Heisenberg ferro- and antiferromagnets on simple and body-centered cubic lattices for $S = 1/2, 1, 3/2$. The computed $T_c(S)$ can be accurately fitted to

$$T_c(S) = b_0 S(S+1) + b_1 + \frac{b_2}{S(S+1)} + \dots \quad (7)$$

Here, b_0 coincides with T_c obtained from classical MC simulations, whereas the subsequent terms represent quantum corrections. In all studied cases, the total quantum correction to the transition temperature for $S = 3/2$ amounts to only 3–5%. Independently, the quantum MC simulations of the Heisenberg spin- S antiferromagnet on a square lattice [31] demonstrated a good agreement for $\chi(T)$ and $C(T)$ with classical results for $S \geq 3/2$ and temperatures $T \gtrsim 0.8JS(S+1)$. The similarity between spin correlations of quantum and classical spin models has been revealed in a series of numerical studies [32–36]. Semiclassical dynamics in the $S \geq 1$ magnets with multipolar interactions has also attracted significant recent interest [37–39].

Overall, the classical modeling of the Heisenberg spin systems based on the empirical substitution $S_C = \sqrt{S(S+1)}$ has been widely accepted in the literature. However, in the absence of a definitive result, some studies still adopt $S_C = S$ [40–43], which gives rise to a 30% error in a predicted T_c even for large $S = 5/2$. Furthermore, the correct quantum-classical correspondence for other common terms in the spin Hamiltonians, as, e.g., the single-ion anisotropy, remains completely undiscussed. Nevertheless, a proper inclusion of magnetic anisotropy is indispensable for simulations of the two-dimensional (2D) van der Waals materials [44].

In our work we revisit the problem of quantum-classical mapping for a lattice spin model with *arbitrary* interactions. We prove analytically that in the quantum paramagnetic state the partition function for large spins is given by

$$Z_Q(S) = Z_C(S_C) + O\left(\frac{1}{S_C^2}\right), \quad S_C^2 = S(S+1), \quad (8)$$

where the second term on the rhs represents a quantum correction. The above relation provides a rigorous basis for representing quantum spins with classical vectors of length $S_C = \sqrt{S(S+1)}$ at finite temperatures. It also confirms the empirical formula (7) for the spin dependence of transition temperatures, which has a general validity beyond the nearest-neighbor Heisenberg models studied so far. We demonstrate the capabilities of the classical approach by calculating transition temperatures for several topical magnetic materials with known microscopic interactions and moderate spin values $S = 3/2, 2$, and $5/2$. The transition temperatures obtained from the classical MC simulations agree well with the experimental values. Thus, comparison of computed T_c with

the experimental value provides as a stringent test for any microscopic set of interaction parameters for the spin Hamiltonian of a magnetic material.

The paper is organized as follows. Section II presents our central result: a proof of the asymptotic form of the partition function (8), which establishes the quantum-to-classical mapping for an arbitrary spin system at finite temperatures. Section III describes the classical Monte Carlo simulations performed in our work. The effective classical model is elaborated on in Sec. III A, Sec. III B describes the MC algorithm, and Sec. III C contains results on the transition temperatures of various materials simulated in this study. A brief summary is provided in Sec. IV. Additional information is included in appendices: Appendix A gives an alternative proof of the quantum-to-classical correspondence for spin traces, Appendix B presents a generalization of Marsaglia algorithm used in the MC simulations, and Appendix C describes in detail spin models for each of the studied materials.

II. QUANTUM-TO-CLASSICAL MAPPING

A. Large- S limit of the partition function

We consider a system of N spins with quantum numbers S described by a general Hamiltonian $\hat{\mathcal{H}}$. It is convenient to define a normalized partition function

$$Z = \frac{1}{Z_0} \text{Tr} \{ e^{-\beta \hat{\mathcal{H}}} \}, \quad Z_0 = (2S+1)^N, \quad (9)$$

where $\beta = 1/T$. At infinite temperature ($\beta = 0$), partition functions for quantum and classical spins have the same limiting value of 1, which allows for their direct comparison at finite T . Note that Lieb's theorem (4) does not necessarily hold for an arbitrary form of $\hat{\mathcal{H}}$.

An established technique for computing the partition function Z is the high-temperature expansion in powers of β

$$Z = \sum_{n=0}^{\infty} \frac{(-\beta)^n}{n!} \langle \hat{\mathcal{H}}^n \rangle_0, \quad (10)$$

where $\langle \dots \rangle_0 = (1/Z_0) \text{Tr} \{ \dots \}$ denotes averaging over the uncorrelated paramagnetic state [45–47].

Moments of $\hat{\mathcal{H}}$ in the expansion (10) are expressed as sums over finite lattice graphs, connected or disconnected, which encode different terms of the spin Hamiltonian $\hat{\mathcal{H}}$. The contribution of each graph is split into two factors: a combinatorial lattice-embedding constant and an appropriate multi-spin correlator. Furthermore, spin correlators computed in the ideal paramagnetic state at $\beta = 0$ factorize into traces of products of spin operators with the same lattice index i :

$$K_n(S) = \frac{1}{2S+1} \text{Tr} \{ S_i^{\alpha_1} S_i^{\alpha_2} \dots S_i^{\alpha_n} \}. \quad (11)$$

The number and sequence of operators in each trace are determined by the corresponding lattice graph. On the other hand, the difference between the quantum and classical models comes solely from the spin traces (11). Note that there are also separate high-temperature series for the extensive physical properties, like the free energy $F = -T \ln Z$ or the magnetic susceptibility. These series allow for different variants of the lattice graph counting, including the linked-cluster expansion [46]. These technical details play no role in the following arguments, since the trace evaluation is a necessary step for all of them.

A list of nonzero spin traces (11) for $n \leq 9$ is given in [48]. To elucidate the asymptotic behavior of the partition function $Z_Q(S)$, we now investigate the large- S limit of $K_n(S)$ for arbitrary n . Symmetry arguments based on $SO(3)$ rotations of the spin basis help to identify combinations of spin components that lead to a nonzero trace value [45]. Specifically, the π rotations about the three coordinate axes require that n_x , n_y , and n_z , which represent the *total* numbers of S^x , S^y , and S^z operators, must be either all even or all odd for every nonzero trace. In addition, spin traces with odd n (n_α) have imaginary values in view of the time-reversal symmetry.

Next, we replace S^x and S^y with the ladder operators $S^\pm = S^x \pm iS^y$. Continuous rotations about z change their phases in the opposite way: $S^\pm \rightarrow \exp(\pm i\varphi)S^\pm$. Hence, nonzero traces have an equal number of lowering and raising operators. We now rearrange operators along the string (11) to pair each S^+ with another S^- . Extra terms that appear upon commuting operators have a reduced number of spins and correspond to the sub-leading quantum corrections in the large- S limit. Furthermore, these extra terms also have equal numbers of S^+ and S^- . Substituting

$$S^+S^- = S(S+1) - (S^z)^2 + S^z \quad (12)$$

for each pair of adjacent ladder operators, the original trace $K_n(S)$ can be iteratively expressed as a linear combination of z -traces

$$I_k(S) = \frac{1}{2S+1} \text{Tr}\{(S^z)^k\} = \frac{1}{2S+1} \sum_{m=-S}^S m^k \quad (13)$$

with $k \leq n$ multiplied by powers of $X = S(S+1)$. Since the sum in (13) is nonzero only for even k , the traces $K_n(S)$ with odd n have the subleading dependence on S $K_n(S) = iO(S^{n-1})$.

Sums of powers of the terms of an arithmetic progression (13) are standard mathematical objects. The summation result is expressed via Bernoulli polynomials $B_n(x)$, which are defined by the generating function:

$$\frac{te^{xt}}{e^t - 1} = \sum_{n=0}^{\infty} B_n(x) \frac{t^n}{n!}, \quad (14)$$

see, e.g., [49, 50]. From this definition, it is clear that $B_n(x)$ is a polynomial of degree n with the leading coefficient 1. The sum in (13) is, correspondingly, given

by

$$\sum_{m=-S}^S m^k = \frac{B_{k+1}(S+1) - B_{k+1}(-S)}{k+1}. \quad (15)$$

The rhs of (15) is an odd function of $Y = S+1/2$. Dividing it by $2S+1 = 2Y$ shows that $I_n(S)$ is an even polynomial in Y . Then, by substituting $Y^2 = X+1/4$, we obtain

$$I_n(S) = \frac{X^{n/2}}{n+1} + \sum_{k=1}^{n/2-1} a_k X^k, \quad X = S(S+1). \quad (16)$$

The highest-power term in this expression determines the asymptotic form of $I_n(S)$ in the large- S limit. Another proof of Eq. (16), which uses only elementary functions, is given in Appendix A.

Now, let us consider how the above results change if spin operators are substituted with components of a classical vector of length \tilde{S} , while replacing $\langle \dots \rangle_0$ with a spherical integral normalized to 4π . Spin correlators (11) are now strictly real. Hence, symmetry arguments leave nonzero only the combinations with even powers of each S^α . For the n th power of S^z one finds

$$I_n^C(\tilde{S}) = \int \frac{\sin \theta d\theta d\varphi}{4\pi} (\tilde{S} \cos \theta)^n = \frac{\tilde{S}^n}{n+1}. \quad (17)$$

For $\tilde{S}^2 = S(S+1)$, the integral becomes equal to the leading term in Eq. (16). Since for a classical vector $S^+S^- = \tilde{S}^2 - (S^z)^2$, the leading term equivalence extends to traces involving transverse spin components as well. Hence, in the large- S limit the asymptotic form of an arbitrary trace of operators (11) coincides with the corresponding classical integral for a spin of length

$$S_C = \sqrt{S(S+1)}. \quad (18)$$

In addition, corrections to the asymptotic value can be arranged as an expansion in $1/[S(S+1)]$.

The obtained mathematical result for the spin traces extends, via the lattice graph representation, to each term in the β -expansion of $Z_Q(S)$. This proves the quantum-classical correspondence for the total partition function as long as the high-temperature series converges. Generally, the radius of convergence in β extends from $\beta = 0$ ($T \rightarrow \infty$) to the nearest critical point β_c (T_c). Therefore, the asymptotic form of the partition function (8) or, equivalently, of the free energy $F_Q(S)$, is valid for all temperatures $T > T_c$.

The above proof does not apply for $T < T_c$. However, this does not mean that the classical description breaks down immediately below a phase transition. The renormalization group theory predicts that not only the critical exponents but also the amplitude ratios for various physical observables are fully determined by the universality class of a critical point [51]. Hence, if the effective classical model provides a quantitative description for $T > T_c$, the same must be also correct in the critical region at $T < T_c$.

B. Quantum Corrections

In the paramagnetic phase above T_c , the quantum corrections to the leading asymptotic term in (8) take the form of a series of powers of $1/[S(S+1)]$ with, generally, temperature-dependent coefficients. In principle, this series should converge faster than the standard $1/S$ expansion at $T = 0$. Therefore, quantum spin systems tend to behave more classically at finite temperatures. Consistent with this general trend, a peculiar similarity of spin-spin correlators has been found between a system of quantum spins and its classical counterpart at somewhat higher T for various $S = 1/2$ models in 2D and 3D [33–36]. In a magnetically ordered state below T_c , the quantum corrections break the $1/[S(S+1)]$ scaling exhibiting a crossover to the conventional $1/S$ series at zero temperature. Furthermore, the classical (large- S) limit at $T = 0$ may not be unique, but rather depend on the spin Hamiltonian [39].

Investigating temperature-dependent quantum corrections for spin models both above and below T_c is an interesting problem for future studies. Nevertheless, the formulated approach enables us to derive a simple quantum correction to the magnetic anisotropy in the paramagnetic phase. In the uniaxial case, the anisotropy can be expressed as

$$\hat{\mathcal{H}}_a = D \sum_i \left[(S_i^z)^2 - \frac{1}{3} S(S+1) \right]. \quad (19)$$

The extra constant has no effect on the statistical properties, but ensures that $\langle \hat{\mathcal{H}}_a \rangle_0 = 0$. The high-temperature expansion involves computing the moments of $\hat{\mathcal{H}}_a$ with and without other terms from the spin Hamiltonian. This requires finding the following dimensionless traces

$$I_n^p(S) = \langle \left[(S^z)^2 - \frac{1}{3} X \right]^p (S^z)^n \rangle_0, \quad (20)$$

each associated with a dimensional prefactor D^p and $X = S(S+1)$. In the beginning, let us assume that $p = 1$. Then, for $S = 1/2$, the expression in the square brackets is identically zero. Therefore, the polynomial representation of the spin trace (20) vanishes for $X = 3/4$ and, hence, must contain $(X - 3/4)$ as a factor. It can be combined with the first power of D associated with $I_n^1(S)$ into

$$D_C = D [S(S+1) - 3/4]. \quad (21)$$

This combination naturally appears in the expression for the single-ion contribution to the Curie-Weiss temperature [52].

The goal is to demonstrate now that Eq. (21) is valid for all orders in D and β . To do that we have to check the root multiplicity of $I_n^p(S)$. This is performed by substituting $X \rightarrow X + \varepsilon$ into (20) with $|\varepsilon| \ll 1$. The direct trace evaluation for $S = 1/2$ evidently gives $I_n^p(1/2) \propto \varepsilon^p$. On the other hand, the same result follows from a general

polynomial form of $I_n^p(S, \varepsilon)$ only if the root $X = 3/4$ has a multiplicity p :

$$I_n^p(S) = (X - 3/4)^p f(X). \quad (22)$$

Hence, the combination (21) appears in all terms of the high-temperature series and, thus, determines the anisotropy constant D_C for the effective classical model. The constant vanishes for $S = 1/2$, satisfying the necessary physical requirement. In a sense, the renormalization (21) at high temperatures resembles the substitution $D \rightarrow D[1 - 1/(2S)]$ in the spin-wave expression for the anisotropy gap of the easy-axis ferro- or antiferromagnets at $T = 0$ [53, 54].

To conclude this section, we note that representation of the spin traces as polynomials in $X = S(S+1)$ is well-known in the literature [45, 55]. From a symmetry point of view, it is obviously related to the fact that the $SO(3)$ group has the single Casimir operator [56]. However, to the best of our knowledge, neither a proof of the universal match between the leading term in $I_n(S)$ and the classical result (17), nor its implication for the quantum-classical correspondence have been published before. The effective classical model can be further studied using Monte Carlo simulations [19]. This approach is a versatile and often more convenient alternative to the direct high-temperature expansion, which becomes overly complicated for models with multiple exchanges. In the next section, we demonstrate the predictive power of the quantum-to-classical mapping by performing MC simulations of realistic spin models for several topical materials.

III. MONTE CARLO SIMULATIONS

A. Effective classical model

Consider a generic spin- S Hamiltonian with arbitrary exchange interactions, the single-ion anisotropy and the Zeeman energy:

$$\hat{\mathcal{H}} = \sum_{\langle ij \rangle} J_{ij} \mathbf{S}_i \cdot \mathbf{S}_j + \sum_i \left[D S_i^{z2} - g \mu_B \mathbf{H} \cdot \mathbf{S}_i \right]. \quad (23)$$

Other common interactions, such as the biaxial anisotropy or the biquadratic exchange, can also be included. The classical Monte Carlo (CMC) codes are typically written for unit-length vector spins. Accordingly, the quantum to classical mapping proceeds as

$$\mathbf{S}_i \rightarrow \sqrt{S(S+1)} \mathbf{s}_i, \quad |\mathbf{s}_i| = 1, \quad (24)$$

It gives the following values for the microscopic parameters of the effective classical model:

$$\begin{aligned} J_C &= JS(S+1), & H_C &= g\mu_B H \sqrt{S(S+1)}, \\ D_C &= D[S(S+1) - 3/4]. \end{aligned} \quad (25)$$

According to the arguments of Sec. II B, the anisotropy constant comes with a quantum correction.

In Monte Carlo simulations, it is convenient to use dimensionless spin Hamiltonians. This is achieved by scaling $\hat{\mathcal{H}}$ to the largest exchange constant $J_C = JS(S+1)$. Then, the physical observables are related to their dimensionless Monte Carlo values by

$$k_B T / T_{\text{MC}} = JS(S+1), \quad C / C_{\text{MC}} = k_B N_0, \quad (26)$$

$$M / M_{\text{MC}} = g\mu_B N_0 \sqrt{S(S+1)}, \quad \chi / \chi_{\text{MC}} = \frac{(g\mu_B)^2}{J} N_0.$$

Here, C_{MC} , M_{MC} and χ_{MC} are the heat capacity, the magnetization and the susceptibility normalized per spin, k_B is the Boltzmann constant, μ_B is the Bohr magneton, and N_0 is the Avogadro number.

B. Monte Carlo algorithm

The Monte Carlo simulations have been performed on finite clusters with linear sizes L and periodic boundary conditions. The total number of spins in every cluster is $N = N_c \times L^D$, where N_c is the number of magnetic sites in the crystal unit cell and D is the dimensionality. The MC results presented below were obtained for lattices with up to $N = 5 \times 10^4$ spins. The standard Metropolis algorithm has been used for accepting or rejecting new spin directions. To get better statistics, the acceptance rate was kept at the level of 30–50% for all temperatures. This is usually achieved by restricting variations of z -component of spins in the local frame to $\Delta S^{\text{max}} \simeq T$ [19]. Restricted spin moves have been implemented using modified Marsaglia algorithm [57], see Appendix B for further details.

One Metropolis sweep over the lattice consists of successive attempts to change orientation of every spin. This is followed by microcanonical over-relaxation moves, which further improve statistics of individual MC runs by facilitating a random walk in the phase space [19]. Specifically, the π rotations of spins around their local field directions are used starting with a first randomly chosen spin [58]. One MC step consists of a Metropolis sweep together with five subsequent over-relaxation sweeps. At each temperature, 10^5 MC steps have been performed for equilibration followed by up to 5×10^5 MC steps for measurements. The individual MC runs have been initialized at a high enough temperature $T_{\text{MC}} \simeq 3$ –5 by completely random spin configurations followed by gradual cooling across the simulated temperature range. A total of 100–500 independent MC runs were simulated in parallel on a computer cluster. The presented MC results along with the statistical errors were obtained by averaging the data from different runs.

During MC runs, we compute averages of the internal energy E and squared amplitudes of the Fourier harmon-

ics of the spin density

$$(m_Q^\alpha)^2 = \frac{1}{N^2} \sum_i \langle s_i^\alpha s_j^\alpha \rangle e^{i\mathbf{Q}(\mathbf{r}_i - \mathbf{r}_j)} \quad (27)$$

for the ordering wave-vector(s) \mathbf{Q} of a specific magnetic model. The heat capacity C and the magnetic susceptibility χ are obtained from fluctuations of the internal energy and the magnetization M^α by

$$C = \frac{\langle E^2 \rangle - \langle E \rangle^2}{T^2}, \quad \chi^{\alpha\alpha} = \frac{\langle (M^\alpha)^2 \rangle}{T}. \quad (28)$$

Here, all quantities represent the *total* values for a spin cluster. Additionally, the expression for χ is only valid in a zero magnetic field, when, for a finite system, $\langle M^\alpha \rangle = 0$ at any finite temperature.

In addition, we also compute the fourth-order cumulant for the order parameter

$$U_4 = \frac{\langle m_Q^4 \rangle}{\langle m_Q^2 \rangle^2}. \quad (29)$$

Its application for locating the phase transition points is illustrated in the next subsection.

C. Monte Carlo results

In this subsection we present the Monte Carlo results for a few selected ferro- and antiferromagnetic materials with spin (angular momentum) values $S = 3/2$, 2, and 5/2. Specifically, we have performed simulations for MnF_2 , MnTe , Rb_2MnF_4 , MnPSe_3 , FePS_3 , FePSe_3 , CoPS_3 , CrSBr , and CrI_3 . The details of the corresponding spin models together with values of the interaction constants are presented in Appendix C.

We begin with the transition temperatures. Due to the rounding effects on finite lattices, the peak position in the specific heat is a rather poor method for locating T_c . The fourth-order cumulants of the order parameter (29) provide instead an accurate approach that does not require prior knowledge of the critical exponents. The scale-invariance hypothesis suggests the following form of U_4 as a function of distance to the critical point $\tau = (T - T_c)/T_c$ and system's linear size L :

$$U_4(\tau, L) = f(\tau L^{1/\nu}), \quad (30)$$

where $f(x)$ is a universal function [19]. Therefore, plots of $U_4(T)$ for different system sizes L intersect near T_c . The corrections to the true crossing appear due to small corrections to the above scaling form. Below, we give two illustrations of the application of this method.

Figure 1(a) shows the cumulant plot used to locate the transition temperature T_c of MnF_2 . This collinear easy-axis antiferromagnet on a body-centred tetragonal lattice is described by a scalar order parameter m_q^z with $\mathbf{q} = (\pi, \pi, \pi)$. The spin model of MnF_2 , see Appendix C

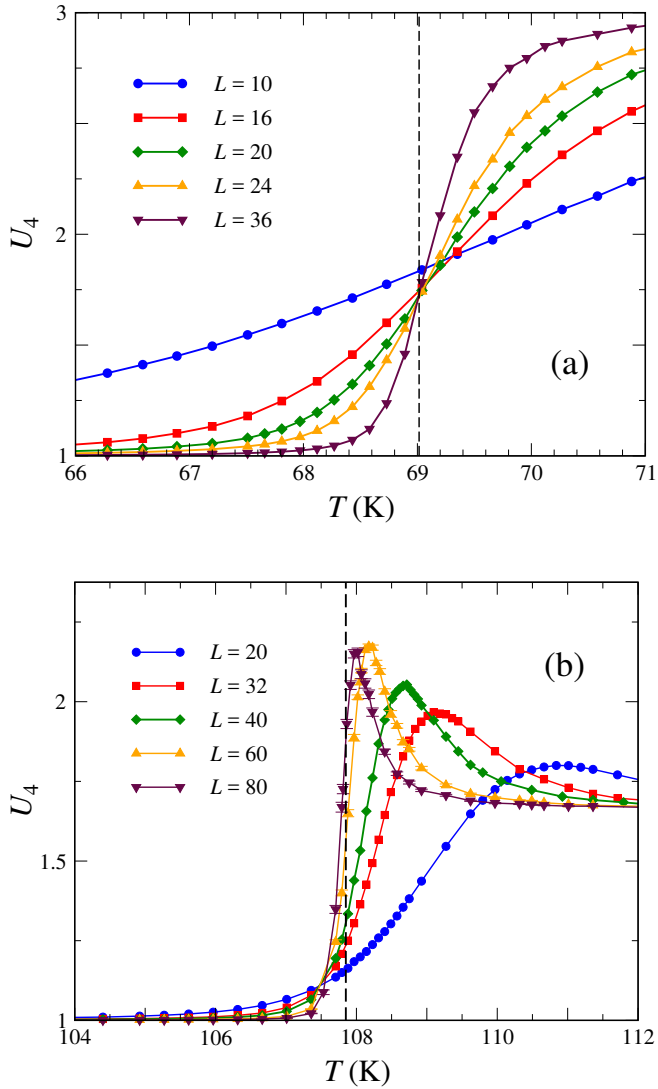


FIG. 1. Fourth-order cumulants versus temperature for the spin models of MnF_2 (a) and FePSe_3 (b). Phase transition temperatures are indicated by dashed lines. If not shown, the error bars are smaller than the symbol sizes.

for details, have been simulated on periodic lattices with $N = L^3$ spins and $L = 10\text{--}36$. For $T \gg T_c$, the cumulants are close to $U_4 = 3$ consistent with the Gaussian fluctuations of the order parameter. Below transition, m_q^z is finite and $U_4 = 1$. The cumulants vary monotonically between these two limiting values crossing at $T_c = 69.01$ K. The crossing point of $U_4(T, L)$ is rather tight and allows us to estimate T_c with high precision without further finite-size scaling of the individual crossing points.

For the second example we choose the van der Waals material FePSe_3 . This collinear honeycomb antiferromagnet has a strong easy-axis anisotropy, which allows us to study its phase transition in a simplified 2D spin model, see Appendix C. The in-plane zigzag antiferromagnetic order in FePSe_3 breaks the C_3 rotation symme-

try of the honeycomb lattice and has a three-component order parameter corresponding to the M point in the hexagonal Brillouin zone. Figure 1(b) shows the fourth-order cumulants obtained by simulating periodic lattices with $N = 2L^2$ spins, $L = 20\text{--}80$. For an n -component vector order parameter, above T_c each component fluctuates independently resulting in $U_4 \approx (n + 2)/n$. Accordingly, the cumulants approach $5/3$ ($n = 3$) at high temperatures, see Fig. 1(b).

Unlike MnF_2 , the cumulants for FePSe_3 exhibit a non-monotonic dependence on T with a peak singularity for $L \rightarrow \infty$. The nonmonotonic behavior of the fourth-order cumulants signifies the first-order transition [59–61]. Such a dependence of $U_4(T, L)$ is related to a double peak structure in the probability distribution of the order parameter characteristic for the phase coexistence [59]. By extrapolating the peak position versus $1/N \rightarrow 0$, we determine the transition temperature $T_c = 107.8 \pm 0.1$ K. The natural question that arises now is why does the six-fold ($2n = 6$) symmetry breaking in FePSe_3 occur via the first-order transition?

Generally, phase transitions with the Z_n symmetry breaking can belong to either the n -state Potts or the n -state clock universality classes. A simple geometrical analysis of the domain walls between the C_3 rotated zigzag antiferromagnetic states suggests a similarity with the Potts model. Furthermore, the six-state Potts model has a first-order transition in 2D [62], whereas the six-state clock model exhibits two successive Kosterlitz-Thouless transitions [63]. Therefore, FePSe_3 provides a rare realization of the 2D spin system in the six-state Potts universality class [64]. The recent experimental study has clearly demonstrated the first-order nature of the phase transition in FePSe_3 [65] in full agreement with our theoretical result.

Monte Carlo simulations and their detailed data analysis have been performed for each of the selected materials. The computed transition temperatures are presented in Table I. In addition, Table gives a brief information about the spin model for each material with corresponding references, see Appendix C for further details. Together with the MC result T_c^{MC} and the measured value T_c^{exp} we also provide a mean-field estimate for the transition temperature:

$$k_B T_c^{\text{MF}} = -\frac{1}{3} S(S + 1) \sum_{\mathbf{r}} J_{ij} e^{-i\mathbf{Q} \cdot \mathbf{r}_{ij}}. \quad (31)$$

where \mathbf{Q} is the ordering wavevector and \mathbf{r}_{ij} are inter-site distances, see, for example, [31, 83]. As expected, the mean-field approximation always overestimates the transition temperatures. The actual error widely varies between 25% for the 3D spin model of MnF_2 with the high coordination number $z = 8$ to 100% in the case of the 2D easy-axis model of Rb_2MnF_4 with the low coordination number $z = 4$.

Material	Spin Model	Method	T_c^{MF} (K)	T_c^{MC} (K)	T_c^{exp} (K)
MnF_2 , $S = 5/2$ easy-axis, 3D	$\{J_1, J_2, J_3, D\}$	INS [14] + ESR [66]	87	69	67.7 [67]
MnTe , $S = 5/2$ easy-plane, quasi-1D	$\{J_1, J_2, J_3, D\}$	INS [13]	486	359	310 [68]
		DFT [69] + ESR [70]	415	300	
MnPSe_3 , $S = 5/2$ easy-plane XXZ, quasi-2D	$\{J_1, J_2, J_3, J_c\}$	powder INS [6]	145	73	74 [71]
	$\{J_1, J_1^{zz}, J_2, J_3, J_c\}$	INS [72]	119	77	
Rb_2MnF_4 , $S = 5/2$ easy-axis XXZ, 2D	$\{J_1, J_1^{zz}\}$	INS [73]	91	41	38.4 [74]
FePS_3 , $S = 2$ easy-axis, 2D	$\{J_1, J_2, J_3, D\}$	INS [75]	205	142	118 ± 1 [76]
	$\{J_{1a}, J_{1b}, J_2, J_3, D\}$	INS [5]	212	130	
FePSe_3 , $S = 2$ easy-axis, 2D	$\{J_1, J_2, J_3, D\}$	ESR [77]	151	108	106 ± 1 [76]
	$\{J_1, J_2, J_3, D\}$	INS [65]	183	134	
CoPS_3 , $S = 3/2$ bi-axial, 2D	$\{J_1, J_2, J_3, D, E\}$	INS [12]	153	113	119.1 [78]
CrSBr , $S = 3/2$ bi-axial, quasi-2D	$\{J_1, J_2, J_3, J_c, D, E\}$	INS [8] + ESR [11]	300	166 ± 3	132 [79]
CrI_3 , $S = 3/2$ easy-axis, quasi-2D	$\{J_1, J_2, J_3, J_{c1}, J_{c2}, D\}$	INS [7]	97	67 (bulk) 46 (ML)	61 [80, 81] 45 [82]

TABLE I. Computed and measured transition temperatures for selected magnetic materials. The first column presents the chemical formula, spin value, type of anisotropy and dimensionality. The second and third columns provide the microscopic spin model and method used to obtain the interaction parameters. Here, INS and ESR denote the inelastic-neutron scattering and the electron-spin resonance experiments, whereas DFT stands for the density-functional calculations. The last three columns list transition temperatures from mean-field calculations T_c^{MF} , classical Monte Carlo simulations T_c^{MC} (both this work) and experimentally measured T_c^{exp} . Unless specified, the accuracy of T_c value is less than the last shown digit.

Now, let us compare the MC results for the transition temperatures with their experimental values. For majority of studied models, the agreement between theory and experiment is good with differences between the two values being of the order of 3–6%. Perhaps, the most spectacular example is MnF_2 , for which the discrepancy is smaller than 2%. This puts MnF_2 as an antiferromagnetic material with the best known set of interaction constants. The computed and measured transition temperatures are also in a good agreement for FePSe_3 for a set of microscopic constants from [77]. The correspondence worsens for an alternative set from the INS study [65]. Of course, one cannot claim that one set of interaction constants is superior to another based solely on T_c values. However, calculated transition temperatures provide an additional criterion for selecting among multiple sets of parameters.

A good match between theory and experiment is also found for MnPSe_3 , Rb_2MnF_4 , CoPS_3 , and the monolayer of CrI_3 , see Table I. The worst agreement has been obtained for CrSBr with the mismatch between two T_c ’s of the order of 25%. Regarding a possible role of quantum effects for such a discrepancy, we note that the computed $T_c^{\text{MC}} = 166$ K exceeds the strongest in-plane exchange $J_2 S(S+1) = 147$ K [8]. In this temperature range, the quantum corrections for a similar 2D spin-3/2 model do not exceed 3–5% both for the specific heat and the susceptibility [31]. Hence, the uncertainties of interaction parameters for the microscopic spin model of CrSBr is a

more plausible source of this disagreement.

However, quantum corrections can become an issue in the vicinity of the ordering temperature of the 2D easy-axis antiferromagnet Rb_2MnF_4 . As further detailed in Appendix C, the computed ordering temperature for Rb_2MnF_4 is $T_c^{\text{MC}} \simeq 0.6JS(S+1)$. At this temperature, differences between the results of quantum and classical MC simulations for the spin-5/2 square-lattice antiferromagnet are at the level of 5% for the magnetic susceptibility and increase to 10–15% for the specific heat [31]. Therefore, Rb_2MnF_4 can serve as a suitable test bed for future studies of temperature-dependent quantum corrections in 2D magnets.

We conclude this section by noting that classical MC simulations can be used not only for determining transition temperatures, but also for other physical properties including the magnetic susceptibility, magnetization and the magnetocaloric effect. The relation between the physical observables and quantities obtained in MC simulations is provided by Eq. (26). Clearly, the quantum low-temperature asymptotes cannot be correctly obtained from classical modeling. Nonetheless, the behavior exhibited at temperatures above and around T_c should be quantitatively comparable to the experimental data.

IV. SUMMARY

Our work investigates the problem of mapping the statistical mechanics of a quantum spin system onto an effective classical model. In the large- S limit, the asymptotic form of the quantum partition function $Z_Q(S, T)$ coincides with the classical one $Z_C(S_C, T)$ for spins of length $S_C = \sqrt{S(S+1)}$. Proving the above results enables one to construct, in principle, a series in powers of $1/S_C^2$ for the thermodynamic properties of a quantum spin model. The first term in the series for any physical observable is given by a classical integral and, hence, can be sampled with the classical MC simulations. We provide classical expressions for standard terms in the spin Hamiltonian (25). In particular, the expression for the magnetic anisotropy constant contains a universal quantum correction. As a corollary to the main result, the transition temperatures of the Heisenberg spin models depend on the spin quantum number S according to (7). To illustrate the predictive power of this approach, the classical MC simulations were performed for several magnetic materials, and the results for their transition temperatures are summarized in Table I.

Finally, we would like to emphasize that our results apply directly to magnetic insulators described by quantum spin Hamiltonians. Metallic materials contain additional interaction terms that describe coupling between localized magnetic moments and band electrons. The presence of these additional energy scales can introduce new crossovers in the paramagnetic state and, undoubtedly, enriches the possible phenomenology.

ACKNOWLEDGMENTS

We are grateful to A. Honecker, D. V. Kveshchenko, M. Orlita, and B. Parisse for valuable discussions. We also thank O. A. Petrenko and T. Ziman for comments and suggestions on the manuscript.

Appendix A: Asymptotic form of spin traces

In this Appendix we show how the asymptotic form of spin traces $I_n(S)$ can be obtained without Bernoulli polynomials using only the elementary mathematical functions. Introducing the generating function

$$I(S, t) = \frac{1}{2S+1} \sum_{m=-S}^S e^{mt}, \quad (\text{A1})$$

we can relate the spin traces to its derivatives at $t = 0$:

$$I_n(S) = \left. \frac{\partial^n}{\partial t^n} I(S, t) \right|_{t=0}. \quad (\text{A2})$$

The geometric series summation yields

$$I(S, t) = \frac{1}{2S+1} \frac{\sinh(S + \frac{1}{2})t}{\sinh t/2} = f(t) g(t), \quad (\text{A3})$$

where

$$f(t) = \frac{\sinh(S + \frac{1}{2})t}{(S + \frac{1}{2})t} = \sum_{p=0}^{\infty} \frac{[(S + \frac{1}{2})t]^{2p}}{(2p+1)!} \quad (\text{A4})$$

and $g(t) = (t/2)/\sinh(t/2)$. Both $f(t)$ and $g(t)$ are even functions and their odd derivatives vanish at $t = 0$. Moreover,

$$f_t^{(2k)}(0) = \frac{(S + \frac{1}{2})^{2k}}{2k+1}. \quad (\text{A5})$$

The binomial expansion of the n -th derivative of (A3) yields $I_n(S)$ as a polynomial of degree $n/2$ in the variable $Z = (S + 1/2)^2$. Then, a substitution $Z = X + 1/4$ is used to rewrite it as a polynomial in $X = S(S + 1)$. Since $g(0) = 1$, the highest degree term is directly given by (A5). Altogether, we obtain the polynomial representation

$$I_n(S) = \frac{X^{n/2}}{n+1} + \sum_{k=1}^{n/2-1} a_k X^k, \quad (\text{A6})$$

which coincides with Eq. (16).

Appendix B: Generalized Marsaglia algorithm

Standard techniques for sampling points from a two-dimensional sphere either require computing trigonometric functions or use three random numbers per point [19]. Marsaglia has suggested an elegant method that generates a uniform distribution of points on a sphere using only two random numbers and no transcendental functions [57]. However, in its original formulation this algorithm is not well-suited for MC simulations of spin models, which generally require restricted spin moves over a sphere. Here, we describe a modified version of Marsaglia algorithm that generates points on a spherical cap of height h .

Suppose the random numbers are uniformly distributed in the interval $x \in (-1, 1)$. The rejection method can be used to generate random points (x_1, x_2) uniformly distributed on a disk by requiring $x_1^2 + x_2^2 \leq 1$. The two derived parameters $r = x_1^2 + x_2^2$ and $\phi = \arg(x_1 + ix_2)$ are uniformly distributed as well: $r \in (0, 1)$ and $\phi \in (0, 2\pi)$. Assigning ϕ to the azimuthal angle of a spin, we express its z -component as

$$S^z = 1 - hr, \quad (\text{B1})$$

which has a uniform distribution on $(1-h, 1)$. Then, the transverse spin components are given by

$$\begin{aligned} S^x &= \cos(\phi) \sqrt{1 - S^{z^2}} = x_1 \sqrt{h(2-hr)}, \\ S^y &= \sin(\phi) \sqrt{1 - S^{z^2}} = x_2 \sqrt{h(2-hr)} \end{aligned} \quad (\text{B2})$$

and, hence, can be computed using only a square-root function. For $h = 2$, the above equation coincides with

the original formula given by Marsaglia [57]. The restricted spin moves used in MC simulations can be generated by fixing the height of a polar cap to the simulation temperature: $h \simeq T$.

Appendix C: Spin models for selected materials

1. MnF₂

MnF₂ is one of the best known examples of the collinear Heisenberg antiferromagnet with large spins $S = 5/2$ of Mn²⁺ ions. It has the body-centered tetragonal crystal structure. Spins in the corners and in the centre of the tetragonal unit cell order in the opposite directions along the c axis below the transition temperature $T_c \simeq 67.7$ K. The microscopic interaction parameters of MnF₂ have been refined by Morano *et al.* [14] with the following values for the three principal exchanges: $J_1 = -0.0677(9)$ meV, $J_2 = 0.3022(6)$ meV, and $J_3 = -0.0044(4)$ meV. In addition, the magnetic anisotropy constant is $D = -0.0267(6)$ meV. The easy-axis anisotropy is responsible for the orientation of the magnetic sublattices along the c axis as well as appearance of a finite magnon gap:

$$\Delta = 2S\sqrt{|D|(J_{\text{eff}} + |D|)}, \quad (\text{C1})$$

where $J_{\text{eff}} = 8J_2$ is a net exchange coupling between two antiferromagnetic sublattices. For the above set of microscopic parameters, one finds $\Delta = 1.277$ meV or 308.8 GHz, which is somewhat larger than the ESR gap $\Delta = 259.7$ GHz [66]. Since, the ESR technique is superior over the inelastic neutron scattering at low energies, we use the ESR gap value $\Delta = 1.074$ meV to refine the anisotropy constant as $D = -0.0189$ meV.

The above value of D together with the quoted exchange parameters from the inelastic neutron-scattering (INS) experiments have been used in our Monte Carlo simulations. We find a good agreement between the experimental $T_c^{\text{exp}} \approx 68$ K and the computed $T_c^{\text{MC}} = 69$ K transition temperatures, which puts MnF₂ as a material with the best known values of microscopic constants in the spin Hamiltonian.

2. MnTe

MnTe is an easy-plane collinear antiferromagnet, which recently attracted attention due to the experimental observation of ‘altermagnetic’ splitting of the magnon bands [13]. It has the hexagonal crystal structure $P6_3/mmc$ and orders at $T_c \simeq 310$ K. In the antiferromagnetic state, manganese spins $S = 5/2$ are parallel inside triangular layers and have the opposite orientation between adjacent layers. According to the INS measurements [13], the principal exchanges are the first-neighbor coupling between layers $J_1 = 3.99$ meV, the nearest-neighbor exchange within each layer $J_2 = -0.12$ meV,

and the next nearest-neighbor exchange between layers $J_3 = 0.472$ meV. In addition, the single-ion anisotropy of the easy-plane type has been determined as $D = 0.0482$ meV. An alternative set of microscopic parameters has been obtained from the density functional (DFT) calculations: $J_1 = 3.628$ meV, $J_2 = 0.078$ meV, and $J_3 = 0.457$ meV [69]. We have used both sets of the exchange constants in our MC simulations. For the DFT set of exchanges, we add the single-ion anisotropy constant derived from the ESR magnon gap $\Delta \approx 3.5$ meV [70] using

$$\Delta = 2S\sqrt{DJ_{\text{eff}}}, \quad (\text{C2})$$

where $J_{\text{eff}} = 2J_1 + 12J_3$ is a net exchange coupling between the opposite magnetic sublattices. The above equation yields $D = 0.0385$ meV.

The transition temperature derived from the MC simulations for the DFT set of parameters $T_c^{\text{MC}} = 300$ K gives a better match of the measured $T_c = 310$ K in comparison to $T_c^{\text{MC}} \simeq 360$ K computed with the INS parameters. Due to the presence of at least four parameters in the spin model of MnTe, we cannot claim superiority of one set of parameters over the other. Instead the example of MnTe again illustrates again our general conclusion that MC simulations of transition temperatures in a magnetic material can be used to scrutinize any suggested set of microscopic parameters obtained from experiments or *ab initio* calculations.

3. Rb₂MnF₄

The square-lattice antiferromagnet Rb₂MnF₄ orders at $T_c = 38.4$ K into a simple Néel structure [74]. The crystallographic structure frustrates exchange coupling between Mn layers and it is reasonable to consider this material as a pure 2D magnet. A weak magnetic anisotropy of Rb₂MnF₄ is predominantly determined by the dipolar interactions and can be approximately modelled using the anisotropic exchange:

$$\hat{\mathcal{H}} = \sum_{\langle ij \rangle} \left[J(S_i^x S_j^x + S_i^y S_j^y) + J^{zz} S_i^z S_j^z \right]. \quad (\text{C3})$$

For values of the nearest-neighbor exchange constants we adopt the INS results: $J = 0.654$ meV, $J^{zz}/J = 1.005$ [73]. The computed transition temperature of Rb₂MnF₄ is $T_c = 41$ K, which amounts to only $T_c \simeq 0.6JS(S+1)$. Based on the comparison of the QMC and CMC results for the Heisenberg spin-5/2 square-lattice antiferromagnet [31], a quantum correction of 5–10% to T_c can be expected in this case, which may explain the difference with the experimental result $T_c = 38.4$ K. In addition, for a better description of the experimental properties of Rb₂MnF₄ one may include the long-range dipolar interactions instead of an effective J^{zz} in Eq. (C3).

4. FePS₃

Antiferromagnet FePS₃ belongs to a large family of layered MPX₃ compounds with X = S, Se [71, 84]. Recently, there was a surge of interest in FePS₃ due to the discovery of antiferromagnetic ordering in monolayer samples of this material [85]. The presence of a finite-temperature transition in a pure 2D spin system becomes possible due to a very large easy-axis anisotropy induced by the crystalline electric field for the $S = 2$ iron magnetic moments. Consequently, an interlayer coupling is often neglected considering FePS₃ as a 2D antiferromagnet on an ideal honeycomb lattice.

Lançon *et al.* [75] used the linear spin-wave fits of the measured magnon dispersion in FePS₃. They deduced in-plane exchange constants up to the third neighbors: $J_1 = -2.92$ meV, $J_2 = 0.08$ meV, $J_3 = 1.92$ meV together with the single-ion anisotropy $D = -2.66$ meV. The interplay of two competing exchanges J_1 and J_3 stabilizes the zig-zag antiferromagnetic structure of iron moments. For collinear easy-axis antiferromagnets, the single-ion anisotropy constant \bar{D} that enters the expression for magnon energies at $T = 0$ is renormalized from its bare value D as $\bar{D} = D[1 - 1/(2S)]$, see, for example, [53, 54]. Finite-temperature Monte Carlo simulations must utilize the bare D . Accordingly, we have employed $D = 4D_{\text{exp}}/3 = -3.55$ meV in Eq. (25) for the effective classical model of FePS₃.

Improved theoretical fits of the same magnon dispersion data for FePS₃ have been obtained by Wildes *et al.* [5] by allowing for inequivalent nearest-neighbor couplings J_{1a} and J_{1b} for parallel and antiparallel pairs of iron spins. The microscopic parameters from the new fits are $J_{1a} = -2.9$ meV, $J_{1b} = -0.7$ meV, $J_2 = 0.094$ meV, $J_3 = 1.28$ meV, and $D = -2.53$ meV. The suggested explanation for such significant difference between J_{1a} and J_{1b} is the presence of a biquadratic exchange

$$\hat{\mathcal{H}}_{\text{biq}} = -K_1 \sum_{\langle ij \rangle} (\mathbf{S}_i \cdot \mathbf{S}_j)^2, \quad (\text{C4})$$

which in the collinear antiferromagnetic states at $T = 0$ produces $J_{1a,b} = J_1 \mp 2K_1 S^2$ for parallel/antiparallel spins. We have simulated the phase transition in FePS₃ using both J_{1a} – J_{1b} and J_1 – K_1 spin models. Table I includes the result of the former model, which agrees better with the experimental T_c .

5. FePSe₃

FePSe₃ is a sister material of FePS₃. The transition temperatures and microscopic values of the in-plane exchange constants are similar for both materials. The infrared absorption measurements by Le Mardelé *et al.* [77] have given the following set of microscopic constants for FePSe₃: $J_1 = -2.5$ meV, $J_2 = 0.5$ meV, $J_3 = 1.0$ meV and $D = -3.7$ meV. An alternative set of the parameters has been obtained in the INS studies [65]:

$J_1 = -2.3$ meV, $J_2 = 0.23$ meV, $J_3 = 2.01$ meV and $D = -2.74$ meV. Again, ferromagnetic J_1 and antiferromagnetic J_3 are the strongest in-plane exchanges. However, in contrast to FePS₃, the second-neighbor exchange J_2 significantly increases in the selenium compound. Our MC simulations of the 2D model for FePSe₃ with the two sets of microscopic constants yield transition temperatures of $T_c = 108$ K and 134 K, respectively, whereas to the experimental value is $T_c = 106$ K [76], , see Table I. Using the spin model of FePSe₃, we have also verified a role of quantum renormalization for the anisotropy constant (21). For $S = 2$, the quantum correction reduces the classical single-ion constant by $\sim 13\%$. Performing MC simulations for the microscopic set [77] without such a correction we have obtained $T_c \approx 113$ K. This result is notably further from the experimental value than the quoted $T_c^{\text{MC}} = 108$ K computed with the correctly rescaled D .

6. MnPSe₃

The hexagonal layers of manganese spin-5/2 ions in MnPSe₃ are stacked in a period-3 structure along the c axis. The collinear antiferromagnetic state in MnPSe₃ has a simple Néel structure indicating a dominant nearest-neighbor exchange $J_1 > 0$. In our MC simulations we have employed two sets of microscopic interaction parameters for MnPSe₃. The first set was suggested by Calder *et al.* [6] based on the powder INS data. It includes the in-plane exchange constants up to the third neighbors: $J_1 = 0.9$ meV, $J_2 = 0.06$ meV, $J_3 = 0.38$ meV, as well as a weak interlayer coupling $J_c = 0.062$ meV. The second set of parameters was put forward by Liao *et al.* [72], who performed INS experiments with single crystals of MnPSe₃: $J_1 = 0.73$ meV, $J_2 = 0.017$ meV, $J_3 = 0.43$ meV, and $J_c = 0.054$ meV. In accordance with the susceptibility measurements, a weak easy-plane anisotropy has been modelled by the XXZ exchange Eq. (C3) on the strongest nearest-neighbor bonds with $J_1^{zz}/J_1 = 0.981$. The two sets of microscopic constants yield transition temperatures of $T_c = 73$ K and 77 K, which are both close to the experimental value $T_c = 74$ K [71].

7. CoPS₃

Spin waves in the single crystals of CoPS₃ have been measured by Wildes *et al.* [12]. They have fitted their data using the microscopic spin-3/2 model with three in-plane exchanges and the bi-axial single ion term

$$\hat{\mathcal{H}}_{\text{SI}} = \sum_i \left[D S_i^{z^2} + E (S_i^{x^2} - S_i^{y^2}) \right], \quad (\text{C5})$$

which is compatible with the overall monoclinic symmetry of CoPS₃ crystals. The linear spin-wave theory yields

$J_1 = -1.37$ meV, $J_2 = 0.09$ meV, and $J_3 = 3.0$ meV with $D = 6.07$ meV and $E = -0.77$ meV for the magnetic anisotropy. Transition temperature obtained in the MC simulations with the above set of microscopic constants $T_c = 113$ K compares favorably with the experimental value $T_c = 119$ K [78].

8. CrSBr

CrSBr is the spin-3/2 van der Waals material. It has an orthorhombic crystal structure with ferromagnetically ordered *ab* layers of Cr ions stacked antiferromagnetically in the *c* direction. The in-plane exchange interactions up to the eight neighbors have been obtained from the INS measurements in [8]. The three largest exchange constants are $J_1 = -1.9$ meV, $J_2 = -3.38$ meV, and $J_3 = -1.67$ meV. The other in-plane exchanges are small and do not exceed 5-10% of the dominant J_2 constant. The accuracy of the neutron experiments is insufficient to determine much weaker interlayer exchange coupling as well as the anisotropy constants. These parameters have been measured in the ESR experiments. In particular, the interlayer exchange is estimated as $J_c = 0.0694$ K or 6.0 μ eV, whereas the bi-axial magnetic anisotropy parameters are given as $D_b = -0.3956$ K and $E_{ca} = 0.2074$ K [11]. Here, D_b describes the easy-axis anisotropy for the *b* direction, while E_{ac} parameterizes anisotropy between the hard *c* direction and the intermediate *a* axis. The energy scale hierarchy becomes more transparent if one uses instead the parameterization similar to (C5) with D_c and E_{ab} . A simple geometrical transformation yields $D_c = 0.509$ K or 43.9 μ eV and $E_{ab} = 0.094$ K or 8.1 μ eV. Thus, the magnetic anisotropy of CrSBr is predominantly of the easy-plane type with a weak in-plane anisotropy between the *a* and

b directions. This rather weak easy-axis anisotropy together with inter-plane J_c , which are three orders of magnitude smaller than the principal exchange, play an essential role in the three-dimensional magnetic ordering in CrSBr. The computed transition temperature is $T_c = 166$ K $\simeq J_2 S(S+1) = 147$ K. The quantum effects at corresponding temperatures should be *a priori* small. Therefore, the difference with the experimental value $T_c = 132$ K [79] may come from uncertainties for the in-plane exchange constants.

9. CrI₃

CrI₃ is a prominent example of van der Waals honeycomb-lattice material, which exhibits ferromagnetism down to monolayer limit [82]. Being a promising candidate for spintronics applications, CrI₃ has also attracted attention due to possible realization of topological magnon bands [86]. We use in our MC simulations of CrI₃ the following set of microscopic constants : $J_1 = -2.11$ meV, $J_2 = -0.11$ meV, and $J_3 = 0.1$ meV for the intra-layer exchanges, the anisotropy constant $D = -0.123$ meV and two inter-layer exchanges $J_{c1} = 0.048$ meV and $J_{c2} = -0.071$ meV [7]. The single-ion anisotropy plays an essential role in stabilizing the Ising-type of ferromagnetic order in 2D layers. We renormalize the experimental value of D using the same procedure as discussed in the subsection for FePS₃. For simulations of the phase transition in the mono-layer sample we use the same bulk values of the in-plane exchange constants. Ferromagnetic transition for a single layer is reproduced with very good accuracy. An error of 10% between theoretical and experimental T_c for bulk samples may be assigned to the remaining uncertainty in the values of inter-plane exchange.

[1] R. Coldea, D. A. Tennant, K. Habicht, P. Smeibidl, C. Wolters, and Z. Tylczynski, Direct measurement of the spin Hamiltonian and observation of condensation of magnons in the 2D frustrated quantum magnet Cs₂CuCl₄, *Phys. Rev. Lett.* **88**, 137203 (2002).

[2] J. Zhao, D.-X. Yao, S. Li, T. Hong, Y. Chen, S. Chang, W. Ratcliff, J. W. Lynn, H. A. Mook, G. F. Chen, J. L. Luo, N. L. Wang, E. W. Carlson, J. Hu, and P. Dai, Low energy spin waves and magnetic interactions in SrFe₂As₂, *Phys. Rev. Lett.* **101**, 167203 (2008).

[3] L. Savary, K. A. Ross, B. D. Gaulin, J. P. C. Ruff, and L. Balents, Order by quantum disorder in Er₂Ti₂O₇, *Phys. Rev. Lett.* **109**, 167201 (2012).

[4] H. Jacobsen, S. M. Gau, A. J. Princep, E. Hamilton, S. Tóth, R. A. Ewings, M. Enderle, E. M. H. Wheeler, D. Prabhakaran, and A. T. Boothroyd, Spin dynamics and exchange interactions in CuO measured by neutron scattering, *Phys. Rev. B* **97**, 144401 (2018).

[5] A. R. Wildes, M. E. Zhitomirsky, T. Ziman, D. Lançon, and H. C. Walker, Evidence for biquadratic exchange in the quasi-two-dimensional antiferromagnet FePS₃, *J. Appl. Phys.* **127**, 223903 (2020).

[6] S. Calder, A. V. Haglund, A. I. Kolesnikov, and D. Mandrus, Magnetic exchange interactions in the van der Waals layered antiferromagnet MnPSe₃, *Phys. Rev. B* **103**, 024414 (2021).

[7] L. Chen, J.-H. Chung, M. B. Stone, A. I. Kolesnikov, B. Winn, V. O. Garlea, D. L. Abernathy, B. Gao, M. Augustin, E. J. G. Santos, and P. Dai, Magnetic field effect on topological spin excitations in CrI₃, *Phys. Rev. X* **11**, 031047 (2021).

[8] A. Scheie, M. Ziebel, D. G. Chica, Y. J. Bae, X. Wang, A. I. Kolesnikov, X. Zhu, and X. Roy, Spin waves and magnetic exchange Hamiltonian in CrSBr, *Adv. Sci.* **9**, 2202467 (2022).

[9] Y. Gu, Q. Wang, H. Wo, Z. He, H. C. Walker, J. T. Park, M. Enderle, A. D. Christianson, W. Wang, and J. Zhao, Frustrated magnetic interactions in FeSe, *Phys. Rev. B* **106**, L060504 (2022).

[10] A. Scheie, P. Laurell, P. A. McClarty, G. E. Granroth, M. B. Stone, R. Moessner, and S. E. Nagler, Spin-exchange Hamiltonian and topological degeneracies in elemental gadolinium, *Phys. Rev. B* **105**, 104402 (2022).

[11] C. W. Cho, A. Pawbake, N. Aubergier, A. L. Barra, K. Mosina, Z. Sofer, M. E. Zhitomirsky, C. Faugeras, and B. A. Piot, Microscopic parameters of the van der Waals Cr₃Br₄ antiferromagnet from microwave absorption experiments, *Phys. Rev. B* **107**, 094403 (2023).

[12] A. R. Wildes, B. Fåk, U. B. Hansen, M. Enderle, J. R. Stewart, L. Testa, H. M. Rønnow, C. Kim, and J.-G. Park, Spin wave spectra of single crystal CoPS₃, *Phys. Rev. B* **107**, 054438 (2023).

[13] Z. Liu, M. Ozeki, S. Asai, S. Itoh, and T. Masuda, Chiral split magnon in altermagnetic MnTe, *Phys. Rev. Lett.* **133**, 156702 (2024).

[14] V. C. Morano, Z. Maesen, S. E. Nikitin, J. Lass, D. G. Mazzone, and O. Zaharko, Absence of altermagnetic magnon band splitting in MnF₂, *Phys. Rev. Lett.* **134**, 226702 (2025).

[15] K. Riedl, Y. Li, R. Valentí, and S. M. Winter, Ab initio approaches for low-energy spin Hamiltonians, *Phys. Stat. Solidi (b)* **256**, 1800684 (2019).

[16] A. Szilva, Y. Kvashnin, E. A. Stepanov, L. Nordström, O. Eriksson, A. I. Lichtenstein, and M. I. Katsnelson, Quantitative theory of magnetic interactions in solids, *Rev. Mod. Phys.* **95**, 035004 (2023).

[17] A. W. Sandvik, Computational studies of quantum spin systems, *AIP Conf. Proc.* **1297**, 135 (2010).

[18] J. Gubernatis, N. Kawashima, and P. Werner, *Quantum Monte Carlo Methods* (Cambridge University Press, Cambridge, 2016).

[19] D. P. Landau and K. Binder, *A Guide to Monte Carlo Simulations in Statistical Physics* (Cambridge University Press, Cambridge, 2000).

[20] P. J. Brusgaard and H. A. Tolhoek, Classical limits of Clebsch-Gordan coefficients, Racah coefficients and $D_{mn}^l(\phi, \theta, \psi)$ -functions, *Physica* **23**, 955 (1957).

[21] L. G. Yaffe, Large N limits as classical mechanics, *Rev. Mod. Phys.* **54**, 407 (1982).

[22] M. E. Fisher, Magnetism in one-dimensional systems — the Heisenberg model for infinite spin, *Am. J. Phys.* **32**, 343 (1964).

[23] K. Millard and H. S. Leff, Infinite-spin limit of the quantum Heisenberg model, *J. Math. Phys.* **12**, 1000 (1971).

[24] J. G. Conlon and J. P. Solovej, On asymptotic limits for the quantum Heisenberg model, *J. Phys. A* **23**, 3199 (1990).

[25] T. Holstein and H. Primakoff, Field dependence of the intrinsic domain magnetization of a ferromagnet, *Phys. Rev.* **58**, 1098 (1940).

[26] A. Auerbach, *Interacting Electrons and Quantum Magnetism* (Springer-Verlag, New York, 1994).

[27] E. H. Lieb, The classical limit of quantum spin systems, *Commun. Math. Phys.* **31**, 327 (1973).

[28] T. Huberman, D. A. Tennant, R. A. Cowley, R. Coldea, and C. D. Frost, A study of the quantum classical crossover in the spin dynamics of the 2D $S = 5/2$ antiferromagnet Rb₂MnF₄: neutron scattering, computer simulations, and analytic theories, *J. Stat. Mech.* **2008**, P05017 (2008).

[29] D. Dahlbom, F. T. Brooks, M. S. Wilson, S. Chi, A. I. Kolesnikov, M. B. Stone, H. Cao, Y.-W. Li, K. Barros, M. Mourigal, C. D. Batista, and X. Bai, Quantum-to-classical crossover in generalized spin systems: Temperature-dependent spin dynamics of FeI₂, *Phys. Rev. B* **109**, 014427 (2024).

[30] J. Oitmaa and W. Zheng, Curie and Néel temperatures of quantum magnets, *J. Phys.: Condens. Matter* **16**, 8653 (2004).

[31] D. C. Johnston, R. J. McQueeney, B. Lake, A. Honecker, M. E. Zhitomirsky, R. Nath, Y. Furukawa, V. P. Antropov, and Y. Singh, Magnetic exchange interactions in BaMn₂As₂: A case study of the J_1 - J_2 - J_c Heisenberg model, *Phys. Rev. B* **84**, 094445 (2011).

[32] N. Elstner, A. Sokol, R. R. P. Singh, M. Greven, and R. J. Birgeneau, Spin dependence of correlations in two-dimensional square-lattice quantum Heisenberg antiferromagnets, *Phys. Rev. Lett.* **75**, 938 (1995).

[33] S. A. Kulagin, N. Prokof'ev, O. A. Starykh, B. Svistunov, and C. N. Varney, Bold diagrammatic Monte Carlo method applied to fermionized frustrated spins, *Phys. Rev. Lett.* **110**, 070601 (2013).

[34] Y. Huang, K. Chen, Y. Deng, N. Prokof'ev, and B. Svistunov, Spin-ice state of the quantum Heisenberg antiferromagnet on the pyrochlore lattice, *Phys. Rev. Lett.* **116**, 177203 (2016).

[35] T. Wang, X. Cai, K. Chen, N. V. Prokof'ev, and B. V. Svistunov, Quantum-to-classical correspondence in two-dimensional Heisenberg models, *Phys. Rev. B* **101**, 035132 (2020).

[36] B. Schneider and B. Sbierski, Taming spin susceptibilities in frustrated quantum magnets: Mean-field form and approximate nature of the quantum-to-classical correspondence, *Phys. Rev. Lett.* **134**, 176502 (2025).

[37] H. Zhang and C. D. Batista, Classical spin dynamics based on SU(N) coherent states, *Phys. Rev. B* **104**, 104409 (2021).

[38] K. Remund, R. Pohle, Y. Akagi, J. Romhányi, and N. Shannon, Semi-classical simulation of spin-1 magnets, *Phys. Rev. Res.* **4**, 033106 (2022).

[39] D. A. Dahlbom, H. Zhang, Z. Laraib, D. M. Pajerowski, K. Barros, and C. D. Batista, Renormalized classical theory of quantum magnets, *Phys. Rev. B* **112**, 134432 (2025).

[40] J. Barker and G. E. W. Bauer, Semiquantum thermodynamics of complex ferrimagnets, *Phys. Rev. B* **100**, 140401 (2019).

[41] D. Torelli and T. Olsen, Calculating critical temperatures for ferromagnetic order in two-dimensional materials, *2D Mater.* **6**, 015028 (2019).

[42] A. Kartsev, M. Augustin, R. F. L. Evans, K. S. Novoselov, and E. J. G. Santos, Biquadratic exchange interactions in two-dimensional magnets, *npj Comput. Mater.* **6**, 150 (2020).

[43] T. Olsen, Magnetic anisotropy and exchange interactions of two-dimensional FePS₃, NiPS₃ and MnPS₃ from first principles calculations, *J. Phys. D: Appl. Phys.* **54**, 314001 (2021).

[44] M. Gibertini, M. Koperski, A. F. Morpurgo, and K. S. Novoselov, Magnetic 2D materials and heterostructures, *Nat. Nanotechnol.* **14**, 408 (2019).

[45] G. S. Rushbrooke, G. A. Baker, and P. J. Wood, Heisenberg model, in *Phase Transitions and Critical Phenomena*, Vol. 3, edited by C. Domb and M. S. Green (Academic Press, New York, 1974).

[46] J. Oitmaa, C. Hamer, and W. Zheng, *Series Expansion Methods for Strongly Interacting Lattice Models* (Cam-

bridge University Press, Cambridge, 2006).

[47] B. Tang, E. Khatami, and M. Rigol, A short introduction to numerical linked-cluster expansions, *Comp. Phys. Commun.* **184**, 557 (2013).

[48] E. Ambler, J. C. Eisenstein, and J. F. Schooley, Traces of products of angular momentum matrices, *J. Math. Phys.* **3**, 118 (1962).

[49] M. Abramowitz and I. A. Stegun, eds., *Handbook of Mathematical Functions* (Dover, New York, 1972) Chap. 23.

[50] K. B. Oldham, J. C. Myland, and J. Spanier, *An Atlas of Functions*, 2nd ed. (Springer, Berlin, 2009) Chap. 19.

[51] A. Pelissetto and E. Vicari, Critical phenomena and renormalization-group theory, *Phys. Rep.* **368**, 549 (2002).

[52] Y.-L. Wang, Crystal-field effects of paramagnetic Curie temperature, *Phys. Lett. A* **35**, 383 (1971).

[53] J. Oitmaa and C. J. Hamer, Ground-state properties and one-particle spectra for a spin-1 Heisenberg antiferromagnet from series expansions, *Phys. Rev. B* **77**, 224435 (2008).

[54] A. El Mendili, T. Ziman, and M. E. Zhitomirsky, Longitudinal magnons in large- S easy-axis magnets, *Phys. Rev. B* **112**, 174433 (2025).

[55] N. W. Dalton, Traces of products of angular momentum matrices, *Phys. Lett. A* **28**, 172 (1968).

[56] A. Zee, *Group theory in a nutshell for physicists* (Princeton University Press, Princeton, 2016).

[57] G. Marsaglia, Choosing a point from the surface of a sphere, *Ann. Math. Statist.* **43**, 645 (1972).

[58] K. Kanki, D. Loison, and K. D. Schotte, Efficiency of the microcanonical over-relaxation algorithm for vector spins analyzing first and second order transitions, *Eur. Phys. J. B* **44**, 309 (2005).

[59] M. S. S. Challa, D. P. Landau, and K. Binder, Finite-size effects at temperature-driven first-order transitions, *Phys. Rev. B* **34**, 1841 (1986).

[60] K. Vollmayr, J. D. Reger, M. Scheucher, and K. Binder, Finite size effects at thermally-driven first order phase transitions: A phenomenological theory of the order parameter distribution, *Z. Phys. B* **91**, 113 (1993).

[61] S. Jin, A. Sen, and A. W. Sandvik, Ashkin-Teller criticality and pseudo-first-order behavior in a frustrated Ising model on the square lattice, *Phys. Rev. Lett.* **108**, 045702 (2012).

[62] F. Y. Wu, The Potts model, *Rev. Mod. Phys.* **54**, 235 (1982).

[63] J. V. José, L. P. Kadanoff, S. Kirkpatrick, and D. R. Nelson, Renormalization, vortices, and symmetry-breaking perturbations in the two-dimensional planar model, *Phys. Rev. B* **16**, 1217 (1977).

[64] E. Domany and E. K. Riedel, Phase transitions in two-dimensional systems, *J. Appl. Phys.* **49**, 1315 (1978).

[65] L. Chen, X. Teng, D. Hu, F. Ye, G. E. Granroth, M. Yi, J.-H. Chung, R. J. Birgeneau, and P. Dai, Thermal evolution of spin excitations in honeycomb Ising antiferromagnetic FePSe₃, *NPJ Quantum Mater.* **9**, 40 (2024).

[66] M. Hagiwara, K. Katsumata, I. Yamada, and H. Suzuki, Antiferromagnetic resonance in MnF₂ over wide ranges of frequency and magnetic field, *J. Phys.: Condens. Matter* **8**, 7349 (1996).

[67] J. Strempfer, U. Rütt, S. P. Bayrakci, T. Brückel, and W. Jauch, Magnetic properties of transition metal fluorides MF₂ ($M = \text{Mn, Fe, Co, Ni}$) via high-energy photon diffraction, *Phys. Rev. B* **69**, 014417 (2004).

[68] T. Komatsubara, M. Murakami, and E. Hirahara, Magnetic properties of manganese telluride single crystals, *J. Phys. Soc. Jpn.* **18**, 356 (1963).

[69] I. I. Mazin, Altermagnetism in MnTe: Origin, predicted manifestations, and routes to detwinning, *Phys. Rev. B* **107**, L100418 (2023).

[70] J. Dzian, P. Kubascik, S. Tázlaru, M. Bialek, M. Sindler, F. Le Mardelé, C. Kadlec, F. Kadlec, M. Gryglas-Borysiewicz, K. P. Kluczyk, A. Mycielski, P. Skupinski, J. Hejtmanek, R. Tesar, J. Zelezny, A.-L. Barra, C. Faugeras, J. Volný, K. Uhlirová, L. Nádvorník, M. Veis, K. Výborný, and M. Orlita, Antiferromagnetic resonance in α -MnTe, *Phys. Rev. B* **112**, 024433 (2025).

[71] G. Le Flem, R. Brec, G. Ouvard, A. Louisy, and P. Segransan, Magnetic interactions in the layer compounds MPX₃ ($M = \text{Mn, Fe, Ni}; X = \text{S, Se}$), *J. Phys. Chem. Solids* **43**, 455 (1982).

[72] J. Liao, Z. Huang, Y. Shangguan, B. Zhang, S. Cheng, H. Xu, R. Kajimoto, K. Kamazawa, S. Bao, and J. Wen, Spin and lattice dynamics in the van der Waals antiferromagnet MnPSe₃, *Phys. Rev. B* **109**, 224411 (2024).

[73] R. A. Cowley, G. Shirane, R. J. Birgeneau, and H. J. Guggenheim, Spin fluctuations in random magnetic-nonmagnetic two-dimensional antiferromagnets. I. Dynamics, *Phys. Rev. B* **15**, 4292 (1977).

[74] R. J. Birgeneau, H. J. Guggenheim, and G. Shirane, Neutron scattering investigation of phase transitions and magnetic correlations in the two-dimensional antiferromagnets K₂NiF₄, Rb₂MnF₄, Rb₂FeF₄, *Phys. Rev. B* **1**, 2211 (1970).

[75] D. Lançon, H. C. Walker, E. Ressouche, B. Oulad-diaf, K. C. Rule, G. J. McIntyre, T. J. Hicks, H. M. Rønnow, and A. R. Wildes, Magnetic structure and magnon dynamics of the quasi-two-dimensional antiferromagnet FePSe₃, *Phys. Rev. B* **94**, 214407 (2016).

[76] P. Ferloni and M. Scagliotti, Magnetic phase transitions in iron and nickel phosphorus trichalcogenides, *Thermochim. Acta* **139**, 197 (1989).

[77] F. Le Mardelé, A. El Mendili, M. E. Zhitomirsky, I. Moshelsky, D. Jana, I. Plutnarova, Z. Sofer, C. Faugeras, M. Potemski, and M. Orlita, Transverse and longitudinal magnons in the strongly anisotropic antiferromagnet FePSe₃, *Phys. Rev. B* **109**, 134410 (2024).

[78] A. R. Wildes, V. Simonet, E. Ressouche, R. Ballou, and G. J. McIntyre, The magnetic properties and structure of the quasi-two-dimensional antiferromagnet CoPS₃, *J. Phys.: Condens. Matter* **29**, 455801 (2017).

[79] O. Göser, W. Paul, and H. G. Kahle, Magnetic properties of CrSBr, *J. Magn. Magn. Mater.* **92**, 129 (1990).

[80] M. A. McGuire, H. Dixit, V. R. Cooper, and B. C. Sales, Coupling of crystal structure and magnetism in the layered, ferromagnetic insulator CrI₃, *Chem. Mater.* **27**, 612 (2015).

[81] G. T. Lin, X. Luo, F. C. Chen, J. Yan, J. J. Gao, Y. Sun, W. Tong, P. Tong, W. J. Lu, Z. G. Sheng, W. H. Song, X. B. Zhu, and Y. P. Sun, Critical behavior of two-dimensional intrinsically ferromagnetic semiconductor CrI₃, *Appl. Phys. Lett.* **112**, 072405 (2018).

[82] B. Huang, G. Clark, E. Navarro-Moratalla, D. R. Klein, R. Cheng, K. L. Seyler, D. Zhong, E. Schmidgall, M. A. McGuire, D. H. Cobden, W. Yao, D. Xiao, P. Jarillo-Herrero, and X. Xu, Layer-dependent ferromagnetism in a van der Waals crystal down to the monolayer limit,

[Nature](#) **546**, 270 (2017).

[83] M. E. Zhitomirsky, M. V. Gvozdikova, and T. Ziman, Noncoplanar multi- k states in frustrated spinel and kagome magnets, [Ann. Phys. \(NY\)](#) **447**, 169066 (2022).

[84] R. Brec, Review on structural and chemical properties of transition-metal phosphorus trisulfides MPS_3 , [Solid State Ion.](#) **22**, 3 (1986).

[85] J.-U. Lee, S. Lee, J. H. Ryoo, S. Kang, T. Y. Kim, P. Kim, C.-H. Park, J.-G. Park, and H. Cheong, Ising-type magnetic ordering in atomically thin FePS_3 , [Nano Lett.](#) **16**, 7433 (2016).

[86] S. K. Kim, H. Ochoa, R. Zarzuela, and Y. Tserkovnyak, Realization of the Haldane-Kane-Mele model in a system of localized spins, [Phys. Rev. Lett.](#) **117**, 227201 (2016).